Mixed-phase clouds over the Southern Ocean as observed from satellite and surface based lidar and radar.

Gerald G. Mace[1], Alain Protat[2,3], Sally Benson[1]

1. Department of Atmospheric Sciences, University of Utah
2. Australian Bureau of Meteorology, Melbourne, Australia
3. Australian Antarctic Partnership Program, Institute for Marine and Antarctic Studies, University of Tasmania, Hobart, Australia

Submitted to the Journal of Geophysical Research, January 2021

Corresponding Author Information:
Gerald “Jay” Mace, Professor
Department of Atmospheric Sciences, University of Utah
135 South 1460 East Rm 819 (819 WBB)
Salt Lake City, Utah, 84112-0110
Cell Phone: 801 201 7944
Office Phone: 801 585 9489
Email: jay.mace@utah.edu
Fax: 801 860 0381

Key Points:

1. Based on comparisons with surface-based lidar, lidar observations from above cloud layers significantly undercount the occurrence of mixed phase clouds over the Southern Ocean.
2. A latitudinal gradient in mixed-phase clouds is found in the Southern Ocean associated with the Antarctic Polar Front of the Antarctic Circumpolar Current.
3. Current parameterizations that increase cloud cover by modifying the phase detrainment temperature of shallow convection are not supported by surface observations. An alternate parameterization is suggested.

Abstract: This study investigates the occurrence of mixed-phase clouds (MPC) over the Southern Ocean (SO) using space- and surface-based lidar and radar observations. The occurrence of supercooled clouds is dominated by geometrically thin (< 1km) layers that are rarely MPC. We diagnose layers that are geometrically thicker than 1 km to be MPC approximately 65%, and 4% of the time from below by surface remote sensors and from above by orbiting remote sensors, respectively. We examine the discrepancy in MPC as diagnosed from the below and above. From above, we find that MPC occurrence has a gradient associated with the Antarctic Polar Front near 55°S with the rare occurrence of satellite-derived MPC south of that latitude. In contrast, surface sensors find MPC in 33% of supercooled layers. We infer that space-based lidar cannot identify the occurrence of MPC except when secondary ice-forming processes operate in convection that is sufficiently strong to loft ice crystals to cloud tops. We conclude that the CALIPSO phase statistics of MPC have a severe low bias in MPC occurrence. Based on surface-based statistics, we present a parameterization of the frequency of MPC as a function of cloud top temperature that differs substantially from that used in recent climate model simulations.

Plain Language Summary: Snow in predominantly liquid clouds has important implications for the amount of sunlight absorbed over the high latitude oceans. Particularly over the Southern Ocean, where satellite measurements suggest that ice concentrations are low, knowledge of how often clouds are snowing has critical climate implications. Observations from the surface have high fidelity in identifying snow below cold clouds. We use new measurements collected from Australian research vessels to establish an accurate survey of snow occurrences. We find that the occurrence of snow below cold clouds is much higher than inferred from satellite. We explore reasons for this discrepancy and settle on an explanation that the low concentrations of ice-nucleating aerosol particles result in low concentrations of ice particles except where convective motions are strong enough to create ice particles spontaneously by freezing large drops. We provide a simple temperature-based parameterization of snow occurrence using surface-based measurements.

1. Introduction

The occurrence of ice in subfreezing (hereafter supercooled) liquid phase clouds (hereafter mixed-phase clouds or MPC) exerts significant controls on the energy balance of the Southern Ocean (SO) (Bodas-Salcedo et al., 2016; 2019; Trenberth and Fasullo, 2010). The SO surface energy balance influences phenomena ranging from large-scale ocean circulation to large-scale atmospheric circulations. This includes the sequestering of carbon and heat (Marshall and Speer, 2012; Liu et al., 2018) in the ocean. In the atmosphere, the hemispheric distribution of precipitation is a direct response to the strength of the meridional thermal gradient (Cai et al., 2011; Ceppi and Hartmann, 2015) that is sensitive to the net sunlight absorbed at the ocean surface.

Because the vapor pressure over ice is less than over water in the terrestrial atmosphere, liquid droplets at subfreezing temperatures are unstable in the presence of ice crystals. This instability causes rapid growth of ice particles at the expense of liquid-phase cloud droplets (Bergeron 1935, Findeisen, 1938; Wegener, 1911). Because liquid droplets form on numerous cloud condensation nuclei relative to sparse ice-active nuclei in supercooled clouds (Fossum et al., 2018; McCluskey et al., 2018), the ice that does form tends to precipitate, thereby depleting clouds of liquid water. Cloud dissipation through glaciation reduces cloud areal coverage with a concomitant impact on regional albedo (Vergara-Temprado et al., 2018). Lower cloud cover then exposes the surface ocean to solar radiation that would otherwise have been reflected. The current thinking is that atmospheric models have been too aggressive in forming ice precipitation in SO clouds, resulting in high biases in absorbed sunlight. The simulated meridional temperature gradient that occurs in response to incorrect surface heating in the SO tends to be misplaced and weaker than observed. Errors in the meridional temperature gradient induce a cascade of other biases that range across weather and climate space and time scales (e. g. Schneider and Reusch, 2015).

The recent study of Schneider et al. (2020) exemplifies the far-reaching implications of the cloud phase in SO clouds. Using the most recent version of the Community Earth System Model (Hurrell et al., 2013), Schneider et al (2020) implement a modification to the parameterization of shallow convective clouds that causes those clouds to detrain liquid water instead of ice to lower temperatures. First implemented by Kay et al. (2016) and further evaluated by Frey and Kay (2018), this seemingly minor change results in higher SO cloud cover and reduces the absorbed shortwave bias by a factor of ~4. When coupled with natural stratospheric ozone loss, the CESM 1 with the modified cloud parameterization replicates the observed poleward shift in the mid-latitude westerly jet. The jet stream's increased intensity then increases precipitation over the Antarctic ice sheets by a factor of approximately three compared to a model without the changed cloud parameterization.

Observational studies of the absorbed shortwave bias over the SO have focused on the occurrence frequency of ice-phase precipitation (Bodas-Salcedo et al., 2016, Naud et al. 2014). Satellite data have provided the only broad observations of SO clouds in space and time, although recent shipborne studies have begun to fill in essential gaps (Fossum et al., 2018; Protat et al., 2017; Mace and Protat, 2018; Mace et al., 2020). In particular, the CALIPSO (Winker et al., 2009) and CloudSat (Stephens et al., 2008) satellites have significantly expanded our knowledge of the SO cloud phase. CALIPSO can infer the cloud thermodynamic phase using depolarization. However, this capability is limited to the first three optical depths from the cloud top. We have recently reimagined the algorithm that identifies MPC from CALIPSO data by providing a physical basis for the choice of thresholds where depolarization ratios of backscattered laser light become inconsistent with single-phase liquid clouds (Mace et al., 2020a). In this study, we expand upon Mace et al. (2020a) to further explore the geographic and seasonal distributions of MPC over the SO and their association with oceanographic thermal boundaries.

2. Method and Data Used.

This study uses data from the Calipso and CloudSat satellites and measurements from ship-based depolarization lidar. The surface data were collected during three recent voyages into the SO by Australian research vessels. Because the lidar signal fully attenuates beyond optical depth 3, views of cloud layers from above and below potentially provide very different information about the mixed-phase processes that may be ongoing in a cloud. SO boundary layer clouds typically have optical depths over 3 (Mace et al., 2020). Furthermore, the volume integrated backscatter at lidar wavelengths depends on the relative contributions of the hydrometeors. If the total cross-sectional area of ice crystals is small relative to that of the water droplets, the ice phase's presence may not be detectable. Therefore, it is ambiguous whether layers observed from above have ice in the column that is not sensed by the spaceborne lidar.

On the other hand, surface lidars can sense below cloud base for the presence of precipitating ice crystals that have fallen from the primarily liquid cloud layer. Because ice grows rapidly to large sizes and precipitates, observing from the surface provides unambiguous evidence that mixed-phase processes have been or are ongoing in a cloud layer. In the overwhelming majority of cases, when sub cloud ice precipitation is observed, the cloud layer base shows no evidence of the ice phase precipitation in the depolarization ratio. This is because the water droplets that are typically several orders of magnitude more numerous than the ice crystals dominate the cloud base's light scattering process. We consider the presence of ice below the cloud base as evidence that the layer is mixed-phase. Because the lidar typically attenuates within a few 10's of meters above cloud base when looking from below, we do not attempt to determine where in the layer the ice is present or whether it is present at cloud top.

In 2016 and 2018, the Research Vessel (RV) Investigator collected data from a 355 nm lidar system in campaigns called CAPRICORN I and CAPRICORN II. See Royer et al. 2014 and Mace and Protat (2018) for a brief description of the RMAN lidar system and the CAPRICORN I campaign, while Mace et al. (2020b) describe CAPRICORN 2. CAPRICORN 1 took place in March and April and went as far south as 53°S. During CAPRICORN II, data were collected as far south as the seasonal ice edge during January and February 2018 near 66°S. We also use data from a 532 nm micropulse lidar system from the MARCUS campaign (McFarquhar et al., 2021) that collected data from the RV Aurora Australis from November 2017 through March 2018. We only use MARCUS data collected between early January through March 2018 due to insufficient quality lidar data collected earlier.

Mace and Protat (2018) and Mace et al. (2020b) describe the method used to identify MPC occurrence from the surface-based data. By examining warm layers where ice is not possible and ice-only layers such as snow below cloud base, we identify the depolarization ratio threshold that separates ice hydrometeors from water droplets . Then, for layers with cloud base temperatures below freezing, we reason that because ice hydrometeors grow quickly to large sizes, they would precipitate into the layer below a liquid cloud base. Therefore, we look for precipitation from coincident W-Band radars in the 100 m layer below the cloud base. If the lidar depolarization ratios in the precipitation are consistent with ice, we label the cloud as mixed-phase. Otherwise, we label the cloud as liquid phase. This method of examining the phase of sub cloud precipitation cannot be applied to space-based remote sensors because the lidar signal attenuates in the cloud layers' upper three optical depths.

The lidar on the CALIPSO satellite observes attenuated backscatter in 30 m vertical range bins from 60 m footprints spaced every 300 m along the subsatellite track. The instrument records backscattered light in co- and cross-polarization channels at 532 nm and in the co-polarized channel at 1064 nm. CALIPSO and CloudSat were launched together in April 2006, and they began returning data from within the A-Train satellite constellation by July 2006. From the beginning, operators navigated CloudSat to collect data from along the same ground track as CALIPSO and within a few 10's of seconds spaced in time. The two active remote sensors' data are merged to form a geometric layer characterization product described by Mace and Zhang (2014). For the first year of data collection, CALIPSO pointed 0.3° from nadir but was pointed 3° forward nadir in August 2007 to minimize specular reflection from horizontally oriented ice crystals. In the analysis that follows, we use all day and night data from all longitudes during calendar years 2007 through 2010 between 40°S Latitude and 75°S Latitude.

The phase identification algorithm applied to the CALIPSO data (Mace et al., 2020a) builds on Hu et al. (2009). Hu et al. (2009) examined the layer-integrated co-polar and cross-polar layer-integrated attenuated backscattered laser power from layers that fully attenuate the lidar beam. In Mace et al. (2020a), we use physical reasoning derived from Mie theory to identify when measurements from a supercooled layer are inconsistent with an assumption of liquid-phase droplets. When the temperature of the cloud layer sensed by CALIPSO is colder than the freezing point of water, layers that do not conform to our physical expectations for liquid layers are assumed to depart from this expectation due to the presence of ice crystals immersed in the supercooled liquid. We documented an error rate of less than 0.5% based on known liquid layers that return data in the phase diagram's mixed-phase region. Our methodology differs from that described by Hu et al. (2009), where they use conservative thresholds tuned to the presence of ice-dominant layers. We have established thresholds that identify layers that are inconsistent with single-phase liquid clouds. We also demonstrate through comparison to CloudSat radar reflectivity that such layers are typically due to precipitation-sized ice crystals in the cloudy columns.

3. Results.

Our objective in this study is to document MPC in the SO marine boundary layer (MBL). Therefore, we selectively sample satellite and surface-based data to isolate these layers. We require layers defined by the merged CloudSat and Calipso data to have bases below 2 km and layer tops warmer than -40°C and colder than 0°C. For the surface-based data, we require cloud bases to be colder than freezing and exist below 2 km. For reasons that will become evident, we separate layers by geometric thicknesses of less than 1km, 1-3 km, and 3-5 km. Within each of these thickness categories, we further separate the layers by those precipitating from those not precipitating. We define precipitation as a column-coincident radar reflectivity factor above -15 dBZe.

3.1 Occurrence

Aside from two significant outages in February-March 2009 and in January 2010, we analyze approximately two million merged CALIPSO and CloudSat profiles per month between 40°S Latitude and 75°S Latitude. Approximately 86% of the columns contain a hydrometeor layer.

Approximately ½ of the cloudy columns were composed of a single hydrometeor layer, while ~½ of those composed of clouds that were based in the marine boundary layer. Of the boundary layer clouds, a bit more than half of them were fully attenuating and were, therefore, candidates for the phase estimation algorithm amounting to approximately 16.5M observations over the 48 months. The MBL clouds that were not fully attenuating typically had geometric thicknesses less than 1 km. Of the fully attenuating MBL clouds, ~51% were precipitating (Table 1). Precipitation occurs predominantly in clouds that have a geometric thickness greater than 1 km.

The latitudinal distribution of the ship-based remote sensing data (hereafter surface data) are summarized in Figure 1. The latitudinal distribution of the measurements is unevenly weighted. The maximum in the most southerly latitude bin is because the R/V Aurora Australis spent considerable time at the Mawson, Davis, and Casey Antarctic Stations during the summer resupply activities during the MARCUS campaign, and CAPRICORN I data all occur north of 55°S. The high overall coverage of clouds in the SO and the predominance of low-level clouds is evident. Geometrically thin layers (<1 km thickness) compose the largest fraction of low-level supercooled clouds in the surface data. Differences between the surface and satellite data appear in the fraction of geometrically thin low-level clouds. This difference can be understood by differences in sampling. The satellite data are averaged to 2 km footprints because of the need to combine with CloudSat whereas the surface data sample much smaller regions typically being composed of averages compiled over several tens of seconds. In averaging the satellite data, it is much more likely that the highly reflective surface is sampled. If we remove the requirement that the layers are fully attenuating, both data sets agree that approximately 80% of the cloud occurrence is due to layers less than 1 km thickness based in the MBL. Both data sets also agree that these geometrically thin layers rarely precipitate (18% surface, 14% space), but the precipitation is mostly supercooled liquid when they do.

However, examining the partitioning of phase in the geometrically thin layers, we find a substantial difference between the surface and satellite data. The surface data indicate that 30% of the precipitation from the geometrically thin layers is ice. In contrast, the satellite data essentially diagnose no ice phase to three decimal points in the geometrically thin precipitating clouds. This difference extends to the deeper layers, with just 3% and 9% of the precipitating layers in the 1-3 and 3-5 km thickness bins identified as containing ice. In contrast, the surface data find that 62% and 82% of these columns have ice phase precipitation, respectively. The cause and implications of this difference in MPC occurrence is the primary focus of this study.

Figure 2 expands the summary results in Tables 1 and 2 in terms of the liquid frequency as a function of the layer top temperature. The dominant geometrically thin layer types agree reasonably well between the two data sets. Precipitation remains rare in the geometrically thin layers in both data sets to temperatures approaching -30°C. In the thicker layers, precipitation occurrence increases monotonically as the layer top temperature decreases in both data sets. However, for thicker layers, the phase differences between the two data sets amplify as the layer top temperature decreases, especially for precipitating layers. Somewhat independent of layer thickness, we find that the frequency of MPC in the surface data decreases monotonically from near 1 for the layers near the freezing point to near zero as the layer top temperature approaches -40°C. On the other hand, MPC remains rare in the satellite data for all temperatures down to layer top temperatures approaching -30°C. For temperatures lower

than approximately -30°C, the frequency of liquid begins to decrease substantially in the satellite data as the layer tops cool to near the homogeneous freezing point of water.

The discrepancies between surface-based and space-based MPC occurrence frequencies in the precipitating profiles suggest that CALIPSO cannot sense the presence of some fraction of MPC clouds. We consider two possible reasons. First, the ice hydrometeors not sensed by the space-based lidar may exist at altitudes below which the lidar fully attenuates (typically taken to be optical depth three from the top). Another possibility is that the ice crystals are present in concentrations that are too low to be discriminated from the liquid droplets that dominate the light scattering near the cloud top. Regardless of the reasons, the data suggest that space-based lidar severely undercounts the occurrence frequency of MPC in the supercooled MBL clouds. We next examine the geographic distribution of CALIPSO-observed MPC to shed light on the source of the differences between the surface and satellite data sets.

3.2 Geographic Distribution of Mixed Phase Clouds

One of the intriguing results in Mace et al. (2020a) was a significant latitudinal gradient in MPC over the SO in the CALIPSO data. The ice phase in supercooled liquid clouds near Antarctica was observed to occur much less frequently than in supercooled clouds over warmer waters farther north. In Figure 3, we present a map of MPC occurrence for the 1-3 km thickness clouds with cloud top temperatures between -20°C and 0°C. We choose the 1-3 km thickness range because these clouds precipitate enough to develop useful statistics on MPC occurrence. The temperature range bounds a region where ice nucleating aerosols become increasingly active (McCluskey et al., 2018) while remaining well removed from the homogeneous freezing point. We show the 95% confidence interval distribution (Lancaster, 1961) as a histogram and place contours of this confidence's 25% value on the map. Confidence intervals decrease poleward and equatorward of these contours. We do not plot pixels that have 95% confidence that exceeds 50% of the occurrence frequency. Low values of confidence are due to smaller numbers of this cloud class's occurrences in the latitude and longitude bins. Also plotted in Figure 3 as a red dashed contour is the oceanic Antarctic Polar Front (APF), as reported in Freeman and Lovenduski (2016).

We find that MPC occurrence from CALIPSO in the precipitating 1-3 km clouds has a significant latitudinal gradient increasing in occurrence from just a few percent near the Antarctic continent to values approaching 10% from 45°S and northward. The meridional gradient in MPC is not uniform but demonstrates a weak gradient from the Antarctic coast to about 55°S and then increases much more rapidly northward. The data also suggest a longitudinal asymmetry in the location of the latitudinal gradient. For instance, the maximum gradient magnitude seems to occur closer to 45°S in the Atlantic and Indian sectors. In contrast, the gradient tends to be weaker and displaced to near 55°S in the SO's Pacific sector. The latitudinal gradients are also evident clouds with tops colder than -20C. However, the gradients near the APF is weaker in magnitude. Seasonal maps also demonstrate that the gradient in MPC occurrence in winter is much weaker as clouds in these thickness categories become colder overall.

We note that the longitudinal asymmetry in MPC occurrence closely follows the location of the APF. The APF is just one of several distinct oceanographic fronts that characterize the

eastward flowing Antarctic Circumpolar Current (Sokolov and Rintoul, 2009). The APF has the most distinct surface thermal contrast of these frontal boundaries (Freeman and Lovenduski, 2016). We note from Figure 4 that the APF has similar longitudinal asymmetries with, for instance, a bulge to lower latitudes in the Atlantic and the Indian Ocean and a displacement to higher latitudes in the Pacific. While we do not plot it here, inspection of Figure 4 in Freeman and Lovenduski (2016) shows that the SST gradient's magnitude is strongest in the Atlantic and Indian sectors exceeding 2K/100 km.

In contrast, the SST gradient is weaker and less pronounced where it is displaced further south in the Pacific. As shown in Liu et al. (2011), the APF thermal gradient's variable magnitudes are associated with variations in sensible heat fluxes from the ocean to the atmosphere that is significantly larger in the Atlantic and Indian ocean compared to the Pacific, similar to the magnitudes of the MPC gradients in figure 3. The CALIPSO and CloudSat data's poor sampling statistics make a quantitative evaluation of this apparent association between the gradient magnitudes inconclusive. We can say quantitatively that in a zonal mean, the largest meridional gradient in MPC occurs near 55°S. This Latitude marks the core of the ACC and APF, where SST gradients are largest in a zonal average. The latitudinal dependence in the zonal mean is further illustrated in Figure 4, where we plot the zonally-averaged liquid frequency as a function of cloud top temperature like in Figure 2. The difference between the Northerly and Southerly latitudes is evident. By separating the surface data at the approximate Latitude (52°S) of the APF near the mean longitude of the MARCUS and CAPRICORN campaigns (~140°E) we find that the surface data also show that MPC is more frequent north of the APF for a given cloud top temperature. So, the gradient evident in Figure 2 is likely a physical feature, although the magnitude of MPC's occurrence from above is much lower than what actually occurs.

To understand the discrepancy in MPC occurrence from the surface and satellite observations, suppose we consider the evidence presented thus far. First, overall IN abundance in the SO is very low. McCluskey et al. (2018) suggest that at -10°C IN concentrations are on the order of 1 m^{-3}. Second, we find the latitudinal gradient in MPC in both data sets suggesting that it is an actual feature. Third, we have identified an association between the MPC gradient and the APF thermal boundary. Along and north of the APF, the thermal contrast would induce more vigorous convective motions. These convective motions can loft ice crystals to cloud-top. However, they would also produce ice via secondary ice processes so that the concentration of ice crystals is not limited by the low IN abundance.

Secondary ice production (SIP) is a broad term used to describe a family of microphysical processes that convert water droplets into ice crystals independent of the ice phase's direct or primary nucleation onto IN. See Korolev et al. (2020) for a recent review of SIP. Our contention that SIP is more active along and north the APF is consistent with our understanding of SIP in shallow cumuli. Mossop et al.'s (1970) early paper was based on airborne data collected in winter supercooled boundary layer clouds near Tasmania's western coast. They found that while IN concentrations were a predictor of the occurrence of the ice phase, data from several cumulus penetrations showed ice particle concentrations that were a factor of 10^4 greater than the measured IN concentrations. Earlier reviews of the topic (Mossop, 1986; Pruppacher and Klett, 1997), as well as Korolev et al. (2020), identify the primary SIP mechanisms in supercooled clouds. These include mechanical fracturing of fragile crystals (e. g. Vardiman,

1978; Griggs and Choularton, 1986), freezing and subsequent fracturing of drizzle-sized liquid droplets (e. g. Ono, 1972; Koenig, 1963), and rime splintering (Hallet and Mossop, 1974; Lasher-Trapp et al., 2016). Recently, Keinert et al. (2020) found an enhancement in droplet shattering probability for drizzle droplets composed of a dilute sea salt solution falling at terminal velocity. A rich body of observational (e.g. Lawson et al., 2015; Korolev et al., 2020; Lauber et al., 2018) and theoretical (e. g. Sullivan et al., 2017, 2018) literature exists on this topic. The processes identified are likely all active under the conditions appropriate to their unique physics that require precipitation hydrometeors to be lofted to temperatures between roughly -5°C and -15°C.

The creation and lofting of drizzle-sized droplets and large ice crystals require updrafts of sufficient strength. The terminal velocity of droplets between 300 µm to 1 mm ranges from ~1.2 m s^{-1} to 4 m s^{-1} (Gunn and Kinzer, 1949). For ice crystals to be sensed by the CALIPSO lidar, the updrafts must also have lofted the ice particles to near the tops of the predominantly liquid clouds. While we have no direct measure of updraft speed from the A-Train, we can test the hypothesis that precipitation sized hydrometeors are present when MPC is diagnosed with CALIPSO. We do this by examining coincident radar reflectivity from CloudSat. Figure 5 shows that the predominant liquid water layers tend to have maximum reflectivities that distribute broadly near -10 dBZ. In comparison, layers that have been diagnosed by CALIPSO to be MPC have much higher radar reflectivities that have a narrow peak near +10 dBZ with nearly all observations above 0 dBZ. There is little doubt that nearly all layers diagnosed by CALIPSO to be MPC do contain precipitation-sized hydrometeors.

4. Discussion

In the absence of updrafts of sufficient strength to induce SIP for clouds that are much warmer than the homogeneous freezing temperature of the water, we question whether the observed concentrations of IN in the SO are sufficient to explain the remote sensing measurements. We address this question with a set of simple calculations assuming that the maximum ice crystal concentration would be the maximum IN in the SO reported by M18 (~1 m^{-3} at a temperature of -10°C) as an upper limit. We also assume that the ice crystals form as horizontally oriented plates that reflect laser light perfectly and produce a maximum in lidar backscatter (See Mace et al., 2020a for more discussion). We observe that the modal value of W-band radar reflectivity from CloudSat near MPC layers' tops is near -25 dBZe. We assume that the crystals have the mass- and area dimensional properties of hexagonal ice plates (Mitchell, 1996). We also assume that the crystals have radar backscatter cross-sections approximated by the self-similar Rayleigh-Gans approximation (Hogan and Westbrook, 2014). These volumes would then have a radar reflectivity near -25 dBZe and a concentration of 1 m^{-3} if the plates had a size of approximately 1.3 mm in diameter. To test this, we also used T-matrix as implemented in Hammonds et al. (2014) and obtained a size of 1.1 mm. The layer integrated attenuated backscatter (β) of perfectly reflecting 1.3 mm ice plates must at least equal the backscatter from water droplets (see Hu et al., 2009 their figure 4) in the lidar sample volume. Typical SO liquid clouds have cloud droplet number concentrations above 30 cm^{-3}, (McFarquhar et al., 2020; Mace and Avey, 2017. However, we assume that the liquid droplets that coexist with the ice crystals have a concentration and size of 10 cm^{-3} and 10 µm. If we allow the ice

plates' backscatter efficiency to be 1, then ~8 ice crystals per m^{-3} would be necessary for the ice to have a greater backscatter than the liquid drops. However, the maximum IN in the SO reported by McCluskey et al. (2018) is ~1 m^{-3} at -10°C. Thus, the maximum number of ice crystals formed from IN is more than 8 times smaller than what CALIPSO could observe.

In another limiting calculation, we assume that if the number of perfectly reflecting 1.3 mm plates exists at the maximum concentration reported by McCluskey et al., (2018) then the volume integrated backscatter coefficient would be ~0.006 $(km\ sr)^{-1}$. According to Winker et al. (2009), their figure 4, such a backscatter coefficient would be a factor of 17 below the detection threshold of CALIPSO. The CALIPSO data shows that the average attenuated backscatter in layers that are diagnosed to be MPC and composed of horizontally oriented ice crystals is 0.2 $(km\ sr)^{-1}$. This observed attenuated backscatter is, on average, a factor of 33 greater than would occur if the maximum number possible of INP nucleated and grew to be 1.3 mm plates.

Therefore, it seems that at least an order of magnitude more ice crystals (and probably much more) per unit volume are required than could theoretically be nucleated from primary INP. We emphasize that our calculations are conservative by a substantial amount that we cannot estimate without additional observations. These calculations help us understand the discrepancy between the surface and satellite data. Much lower ice concentrations can be detected from below the cloud, where the hydrometeors have grown to precipitation sizes in their descent through the cloud layer and are not masked by liquid droplets. It remains for future work to quantify the concentration of ice crystals below MPCs in the Southern Ocean.

In Figure 4, we plot the parameterization used by Kay et al. (2016), and Frey and Kay (2017). This parameterization is also denoted as CLDMOD in Schneider et al (2020). That parameterization reasonably represents the occurrence of CALIPSO-derived MPC south of the APF. However, the parameterization produces too little MPC north of the APF. A careful examination of Frey and Kay (2017) their Figure 1 shows that their modified parametrization reduces the positive absorbed shortwave bias poleward of 50°S but the bias become negative (i.e. too much cloud cover) north of 50°S. Similar results can be seen in Varma et al., (2020). We offer the possibility that this response in absorbed shortwave bias is due to more ice and lower cloud cover occurring in the real atmosphere north of the APF than south of it as reported here.

When accounting for the occurrence of MPC from the surface data, it seems clear that the shallow convective detrainment parameterization used in earlier work and plotted in Figure 4 as the dashed black line does not well represent the surface observations. We offer a set of alternative parameterizations that best represent the surface data with values listed in Table 3:

$$f_{region} = f_{warm}; for\ T > T_{ice}$$
$$f_{region} = \frac{(T_{ice} - T)}{M}; for\ T_{cold} < T < T_{ice} \quad \text{Equation 1}$$
$$f_{region} = f_{cold}; for\ T < T_{cold}$$

We plot 1-f_{region} in Figure 4. In the northern region, we suggest two lines valid at different temperatures to best represent the data. If implemented in a model, these new parameterizations would result in decreased cloud cover. The decreased cloud cover would cause a relapse of the surface SW bias at the surface that Kay et al. (2016) attempted to fix via their modified parameterization. We offer a potential solution. As discussed in Frey and Kay

(2017), the primary sink of cloud water detrained from shallow convection is from the conversion of the detrained cloud water to precipitation. Figure 2 shows that the predominant geometrically thin cloud type rarely precipitates down to temperatures as low -30°C. The rarity of precipitation in the geometrically thin layers suggests that loss to precipitation is not rapid. Therefore, these thin layers would be likely to persist in a model and reflect sunlight for a much longer time if the sink to precipitation was reduced. Modifying the loss rate of these shallow clouds to precipitation to better match observations might counter the effect of a more realistic phase parameterization. Experimentation is needed to confirm these speculations. However, as noted in Kay et al. (2016), the simple change that they made to the shallow convective detrainment was meant only to test the sensitivity of the atmosphere to phase, and the goal was to constrain the model based on physical principles eventually. We offer an incremental step in that direction with these results.

5. Conclusions.

A clearer picture of the occurrence of snow in Southern Ocean low-level clouds has emerged from this study. Geometrically thin (<1km) supercooled clouds are rarely mixed-phase, and they dominate the overall coverage of supercooled low cloud layers. Geometrically thicker cloud layers precipitate more often, and that frequency increases with decreasing cloud top temperature. We find that Between 1/3 (surface) to ½ (CALIPSO) of precipitating geometrically thicker layers produce supercooled precipitation. Supercooled liquid drizzle would occur in situations where IN are not active at the cloud temperatures or where updrafts are too weak to loft precipitation to temperatures where secondary ice processes can initiate the ice phase. However, we find a discrepancy between the satellite and surface data in ice phase precipitation frequency. Of the layers that are thicker than 1 km and precipitating, we find that 62% (1-3 km) and 82% (3-5 km) produce ice phase precipitation when viewed from below by lidar, whereas only 3% and 9% show evidence of being MPC when viewed from above by lidar.

We conclude that the rarity and geographic pattern of MPC are due to the limitations of remote sensing MPC layers by nadir-observing lidar. Even in situations where primary IN produces ice, such ice would occur at concentrations that are too low for CALIPSO to distinguish from the background liquid. We contend that the geographic distribution of MPC that we do observe from CALIPSO (Figure 3) is due to the pattern of occurrence of secondary ice processes that become more active in more vigorous convective motions over warmer waters north of the APF. This is supported by the tendency of these MPC columns to have radar reflectivities consistent with the presence of large hydrometeors within strong updrafts. It seems that secondary ice processes that would produce ice in high enough concentrations near cloud top are less active over the relatively colder waters south of the APF, causing MPC to be observed less often by CALIPSO. Based on the measurement statistics from surface-based lidar, low concentration ice precipitation from either primary nucleation mechanisms or weaker secondary processes produces ice precipitation in the more southerly latitudes much more frequently than observed by CALIPSO. However, the ice concentrations at the cloud top are often below the detection threshold of CALIPSO.

These results call into question the phase parameterizations derived for supercooled liquid developed from CALIPSO data. While several studies show that these parameterizations significantly reduce the surface-absorbed shortwave bias in models, we contend that this improvement is for reasons that are not entirely consistent with observations. As evidence for this contention, we observe that while the surface-absorbed shortwave bias is improved south of the APF, the bias often becomes negative north of the APF. This result is consistent with more MPC equatorward of the APF than poleward (Figures 3 and 4). We present an alternate parameterization of MPC that is consistent with the surface observations. Since this new parameterization is sure to cause the surface-absorbed shortwave bias to occur, we offer the possibility, based on observations (Figure 2), that the predominant thin clouds only rarely precipitate. Therefore, these cloud layers are likely to persist for a much longer time than the present parameterizations allow for. Adjusting the liquid water sink processes in the geometrically thin layers to better match observations may be a step toward a more physically-based solution.

A more detailed understanding of the aerosol-cloud-precipitation physics in the remote Southern Ocean is needed. The importance of this region to the global climate is becoming increasingly evident. There are many reasons to expect that this region is both unique on Earth due to the underlying oceanic processes, associated biology, and distance from anthropogenic aerosol sources. The SO is also undergoing broad changes due to a warming climate, recovering ozone, and other forcing factors. A broader understanding of the role of primary and secondary ice processes that create precipitation in the ubiquitous boundary layer clouds that control the albedo and surface energy balance is needed, along with a deeper understanding of the biogeochemical cycles that modulate IN concentrations in the SO. The surface-based data collected between 2016 and 2018 allow us to gain some of that understanding, but the data are sparse in terms of longitude and season. A concerted observational strategy is needed to extend knowledge to the point where we can make definitive statements about the physical processes that control this region's cloud properties.

Acknowledgments: *This research was supported in part by* BER Award DE-SC0018995 (GM and SB) and NASA grants 80NSSC19K1251 (GM and SB). *This project received grant funding from the Australian Government as part of the Antarctic Science Collaboration Initiative program. The Australian Antarctic Program Partnership is led by the University of Tasmania, and includes the Australian Antarctic Division, CSIRO Oceans and Atmosphere, Geoscience Australia, the Bureau of Meteorology, the Tasmanian State Government and Australia's Integrated Marine Observing System. (AP)* Technical, logistical, and ship support for MARCUS were provided by the Australian Antarctic Division through Australia Antarctic Science projects 4292 and 4387 and we thank Steven Whiteside, Lloyd Symonds, Rick van den Enden, Peter de Vries, Chris Young and Chris Richards for assistance. The authors would like to thank the staff of the Marine National Facility for providing the infrastructure and logistical and financial support for the voyages of the RV Investigator. Funding for these voyages was provided by the Australian Government and the U.S. Department of Energy. This work benefited from SST thermal gradient data and help in interpreting the data provided by Natalie Freeman of the University of Colorado, Boulder. Data availability statement: All data used in this study are available in public archives. MARCUS data are available from the DOE ARM archive at https://adc.arm.gov/armlogin/login.jsp, SOCRATES

data are available at https://data.eol.ucar.edu/project/SOCRATES, CAPRICORN I and II data are available at https://doi.org/10.25919/5f688fcc97166.

References:

Bergeron, T.: On the Physics of Cloud and Precipitation, Procès Verbaux de la Séance de VU, GGI à Lisbonne 19S3, Paris, 1935

Bodas-Salcedo, A., P. Hill, K. Furtado, K. Williams, P. Field, J. Manners, P. Hyder, and S. Kato, 2016: Large contribution of supercooled liquid clouds to the solar radiation budget of the Southern Ocean. J. Climate. doi:10.1175/JCLI-D-15- 0564.1

Bodas-Salcedo, A., Mulcahy, J. P., Andrews, T., Williams, K. D., Ringer, M. A., Field, P. R., & Elsaesser, G. S. (2019). Strong dependence of atmospheric feedbacks on mixed-phase microphysics and aerosol-cloud interactions in HadGEM3. Journal of Advances in Modeling Earth Systems, 11, 1735–1758. https://doi.org/10.1029/ 2019MS001688.

Cai, W., P. van Rensch, S. Borlace, and T. Cowan (2011), Does the Southern Annular Mode contribute to the persistence of the multidecade-long drought over southwest Western Australia?, Geophys. Res. Lett., 38, L14712, doi:10.1029/2011GL047943.

Ceccaldi, M., J. Delanoë, R. J. Hogan, N. L. Pounder, A. Protat, and J. Pelon (2013), From CloudSat-CALIPSO to EarthCare: Evolution of the DARDAR cloud classification and its comparison to airborne radar-lidar observations, J. Geophys. Res. Atmos., 118, 7962–7981, doi:10.1002/jgrd.50579.

Ceppi, P. and D. L. Hartmann, 2015: Connections between clouds, radiation, and midlatitude dynamics: A Review. Curr. Climate Change Rep. doi: 10.1007/s40641-015-0010-x.

Cesana, G., and H. Chepfer (2013), Evaluation of the cloud thermodynamic phase in a climate model using CALIPSO-GOCCP, J. Geophys. Res. Atmos., 118, 7922–7937, doi:10.1002/jgrd.50376.

Deppler, S. L., and A. T. Davidson, 2017: Southern Ocean Phytoplankton in a changing climate. Frontiers in Marine Science, doi: 10.3389/fmars.2017.00040.

Field, P. R., Heymsfield, J., Bansemer, A., and Twohy, C. H.: Determination of the combined ventilation factor and capacitance for ice crystal aggregates from airborne observations in a tropical anvil cloud, J. Atmos. Sci., 65, 376–391, 2008.

555 Findeisen, W.: Kolloid-meteorologische Vorgänge bei Neiderschlags-bildung, Meteorol. Z., 55,
556 121–133, 1938
557
558 Freeman, N. M. and N. S. Lovenduski, 2016: Mapping the Antarctic Polar Front: Weekly
559 realizations from 2002-2014. Earth Syst. Sci. Data, 8, 191-198, doi:10.5194/essd-8-191-2016.
560
561 Frenger, I., M. Munnich, N. Gruber, and R. Knutti (2015), Southern Ocean eddy phenomenology,
562 J. Geophys. Res. Oceans, 120, 7413–7449, doi:10.1002/2015JC011047.
563
564 Frey WR, Kay JE (2018) The influence of extratropical cloud phase and amount feedbacks on
565 climate sensitivity. Clim Dyn 50:3097–3116. https ://doi.org/10.1007/s0038 2-017-3796-5
566
567 Fossum, K. N., J. Ovadnevaite, D. Ceburnis, M. Dall'Osto, S. Marullo, M. Bellaicco, R. Simo, D Liu,
568 M Flynn, A. Zuend, and C. O'Dowd, 2018: Summertime primary and secondary contributions to
569 Southern Ocean Cloud Condensation Nuclei, Scientific Reports, 8: 13844, doi:10.1038/s41598-
570 018-32047-4.
571
572 Griggs, D. J., and T. W. Choularton, 1986: A laboratory study of secondary ice particle
573 production by the fragmentation of rime and vapour-grown ice crystals. Quarterly Journal of
574 the Royal Meteorological Society, 112, 149-163.

575 Gunn, R. and G. D. Kinzer, 1949: The terminal velocity of fall for water droplets in stagnant air.
576 Journal of Meteorology, 6, 243-248.

577 Hallet, J. and S. C. Mossop, 1974: Production of secondary ice particles during the riming
578 process. Nature, 249, 26-28.

579 Hammonds, K. D., G. G. Mace, and S. Y. Matrosov, 2014: Approximating the backscatter cross
580 section of ice phase hydrometeor size distributions via a simple scaling of the Clausius-Mossotti
581 factor. Journal of Applied Meteorology and Climatology, 53, 2761-2774.

582 Hogan, R. J., and C. D. Westbrook, 2014: Equation for the microwave backscatter cross section
583 of aggregate snowflakes using the self-similar Rayleigh-Gans approximation. Journal of the
584 Atmospheric Sciences, 71, 3292-3301.

585

586 Hu, Y., et al., 2009: CALIPSO/CALIOP cloud phase discrimination algorithm, Journal of
587 Atmospheric and Oceanic Technology, 26, 2293-2309, DOI: 10.1175/2009JTECHA1280.1

588 Hurrell JW, Holland MM, Gent PR et al (2013) The community earth system model: a framework
589 for collaborative research. Bull Am Meteorol Soc 94:1339–1360. https
590 ://doi.org/10.1175/BAMSD-12-00121 .1
591
592 Kay JE, Wall C, Yettella V et al (2016) Global climate impacts of fixing the southern ocean
593 shortwave radiation bias in the Community Earth System Model (CESM). J Clim 29:4617–4636.
594 https ://doi.org/10.1175/JCLI-D-15-0358.1
595

Keinert, A., D. Spannagel, T. Leisner, A. Kiselev, 2020: Secondary ice production upon freezing of freely falling drizzle drops, Journal of the Atmospheric Science, 77, 2959-2967, DOI: 10.1175/JAS-D-20-0081.1

Koenig, L. R. 1963: The glaciating behavior of small cumulonimbus clouds, J. Atmos. Sci., 20, 29-47, doi:10.1175/1520-0469(1963)020<0029:TGBOSC>2.0.CO:2.

Korolev, A., I. Heckman, J. A. Milbrandt, L. A. Ladino, E. Williams, M. Donovan, and D. J. Smalley 2018: A new look at the environmental conditions favorable to secondary ice production: The melting layer as a potential source, 15th Conference on Cloud Physics, Vancouver, B.C

Korolev, A. and Leisner, T.: Review of experimental studies of secondary ice production, Atmos. Chem. Phys., 20, 11767–11797, https://doi.org/10.5194/acp-20-11767-2020, 2020.

L'Ecuyer, T. S., and J. H. Jiang, 2010: Touring the atmosphere aboard the A-Train, Physics Today, S-0031-9228-1007-020-1, 36-47.

Lancaster, H. O. 1961: Significance tests in discrete distributions, Journal of the American Statistical Association, 56, 223-234.

Lauber, A., A. Kiselev, T. Pander, P. Handmann, and T. Leisner, 2018: Secondary ice formation during freezing of levitated droplets. J. Atmos. Sci., 75, 2815–2826, https://doi.org/10.1175/JAS-D-18-0052.1.

Lasher-Trapp, S., D. C. Leon, P. J. DeMott, C. M. Villanueva-Birriel, A. V. Johnson, D. H. Moser, and C. S. Tully, 2016: A multisensory investigation of rime splintering in tropical maritime cumuli, JAS, 73, 2547-2564, DOI: 10.1175/JAS-D-15-0285.1.

Lawson, R. P., S. Woods, and Hugh Morrison, 2015: The microphysics of ice and precipitation development in tropical cumulus clouds, Journal of the Atmospheric Sciences, 72, 2429-2445, DOI: 10.1175/JAS-D-14-0274.1.

Listowski, C., J. Delanoe, Amelie, Kirchgassner, T. Lachlan-Cope, J. King, 2019: Antarctic clouds, supercooled liquid water and mixed phase, investigated with DARDAR: geographical and seasonal variations.

Liu J., T. Xiao, and L. Chen, 2011: Intercomparison of air-sea heat fluxes over the Southern Ocean. Journal of Climate, 24, 1198-1211, doi: 10.10.1175/2010JCLI3699.1.

Liu, W. J. Lu, S.-P. Xie, and A. Fedorov, 2018: Southern Ocean heat uptake, redistribution, and storage in a warming climate: The role of meridional overturning circulation. Journal of Climate, 31, 4727-4734, doi:10.1175/JCLI-D-17-0761.1.

Mace, G. G. and Zhang, 2014: The Cloudsat Radar-Lidar Geometrical Profile Algorithm (RL-GeoProf): Updates, Improvements, and Selected Results. Journal of Geophysical Research, DOI: 10.1002/2013JD021374.

Mace, G. G., and S. Avey, 2017: Seasonal variability of warm boundary layer clouds and precipitation properties in the Southern Ocean as diagnosed from A-Train data. Journal of Geophysical Res. Atmos., 122, 1015-1032, doi:10.1002/2016JD025348.

Mace, G. G. and A. Protat, 2018: Clouds of the the Southern Ocean from the RV Investigator during CAPRICORN. Part 2: The properties of non precipitating stratocumulus. Journal of Applied Meteorology and Climatology. 57, 1805-1823, DOI: 10.1175/JAMC-D-17-0195.1.

Mace, G. G., Benson, S., & Hu, Y. (2020a). On the frequency of occurrence of the ice phase in supercooled Southern Ocean low clouds derived from CALIPSO and CloudSat. Geophysical Research Letters, 47, e2020GL087554. https://doi.org/10.1029/2020GL087554

Mace, G. G., A. Protat, R. S. Humphries, S. P. Alexander, I. M. McRobert, J. Ward, P. Selleck, M. Keywood, 2020b: Southern Ocean cloud properties derived from CAPRICORN and MARCUS data. Accepted to Journal of Geophysical Reserch.

Marshall, J. and K. Speer, 2012, Closure of the meridional overturning circulation through Southern Ocean upwelling. Nature Geoscience, doi: 10.1038/NGEO1391.

Mitchell, D. L., 1996: Use of mass- and area-dimensional power laws for determining precipitation particle terminal velocities. Journal of the Atmospheric Science, 53, 1710-1273.

Schneider D. P., J. E. Kay, and Jan Lenaerts, 2020: Improved clouds Southern Ocean amplify Antarctic precipitation response to ozone depletion in an earth system model. Climate Dynamics, 55, 1665-1684, doi: 10.1007/s00382-020-05346-8.

McCluskey, C. S., Hill, T. C. J., Humphries, R. S., Rauker, A. M., Moreau, S., Strutton, P. G., et al. (2018). Observations of ice nucleating particles over Southern Ocean waters. Geophysical Research Letters, 45, 11,989–11,997. https://doi.org/10.1029/2018GL079981

McFarquhar, G. and 42 coauthors, 2020: Unique observations of clouds, aerosols, precipitation, and surface radiation over the Southern Ocean: An overview of CAPRICORN, MARCUS, MICRE, and SOCRATES. Bulletin of the American Meteorological Society, Accepted.

Mossop, S. C., A Ono, and E. R. Wishart, 1970, Ice particles in maritime clouds near Tasmania, Quarterly Journal of the Royal Meteorological Society, 96, 487-508.

Mossop, S. C., 1986: The origin and concentration of ice crystals in clouds. Bulletin of the American Meteorological Society, 66(3), 264-273.

Naud, C. M., J. F. Booth, and A. D. Del Genio, 2014: Evaluation of ERA-Interim and MERRA cloudiness in the Southern Ocean. J. Climate, 27, 2109–2124, https://doi.org/10.1175/JCLI-D-13-00432.1.

Ono, A., 1972: Evidence on the nature of ice crystal multiplication processes in natural cloud, J. Rech. Atmos., 6, 399-408.

Protat, A., E. Schulz, L. Rikus, Z. Sun, and Y. Xiao, 2017: Shipborne observations of the radiative effect of Southern Ocean Clouds. J. Geophys. Res. Atmos., 122, 318-328.

Pruppacher, H. R. and J. D. Klett, 1997: Microphysics of Clouds and Precipitation, Kluwer Academic Publishers, 954 pp.

Royer, P., Bizard, A & Sauvage, Laurent & Thobois, Ludovic. (2014). Validation protocol and intercomparison campaigns with the R-MAN 510 aerosol lidar. doi: 10.13140/2.1.4778.1767. Available at https://www.researchgate.net/publication/265087709.

Schneider, D. P. and D. B. Reusch, 2015: Antarctic and Southern Ocean surface temperature in CMIP5 models in the context of the surface energy budget. Journal of Climate, 29, 1689-1715, doi: 10.1175/JCLI-D-15-0429.1.

Schneider, D. P., J. E. Kay, J. Lenaerts, 2020: Improved clouds over Southern Ocean amplify Antarctic precipitation response to ozone depletion in an earth system model. Climate Dynamics, 55:1665-1684, doi:10.1007/s00382-020-05346-8.

Sokolov, S., and S. R. Rintoul (2009), Circumpolar structure and distribution of the Antarctic Circumpolar Current fronts:1. Mean circumpolar paths, J. Geophys. Res., 114, C11018, doi:10.1029/2008JC005108.

Sullivan, S. C., C. Hoose, A. Kiselev, T. Leisner, A. Nenes, 2018: Initiation of secondary ice production in clouds. Atmos. Chem. Phys., 18, 1593-1610, https://doi.org/10.5194/acp-18-1593-2018

Sullivan, S. C., C. Hoose, and A. Nenes, 2017: Investigating the contribution of secondary ice production to in-cloud crystal numbers. Journal of Geophysical Research, Atmospheres, 122, 9391-9412, doi:10.1002/2017JD026546.

Stephens, G. L., et al. (2008), CloudSat mission: Performance and early science after the first year of operation, J. Geophys. Res., 113, D00A18, doi:10.1029/2008JD009982.

Trenberth, Kevin E., John T. Fasullo, 2010: Simulation of Present-Day and Twenty-First-Century Energy Budgets of the Southern Oceans. J. Climate, 23, 440–454. DOI 10.1175/2009JCLI3152.1

Uetake, J. T. C. J. Hill, K. A. Moore, P. J. DeMott, A. Protat, and S. M. Kreidenweis, 2020: Airborne bacteria confirm the pristine nature of the Southern Ocean boundary layer. Proceedings of the National Academy of Sciences, doi: 10.1073/pnas.2000134117.

Vardiman, L. 1978: The generation of secondary ice particles in clouds by crystal-crystal collision. Journal of the Atmospheric Sciences, 35, 2168-2180.

721 Varma, V, O. Morgenstarn, P. Field, K. Furtado, J. Williams, P. Hyder, 2020: Improving the
722 Southern Ocean cloud albedo biases in a general circulation model, Atmos. Chem. Phys, 20,
723 7741-7751, https://doi.org/10.5194/acp-20-7741-2020.

724 Vergara-Temprado, J., A. K. Miltenberger, K. Furtado, D. P. Grosveno, B. J. Shipway, A. A. Hill, J.
725 M. Wilkinson, P. R. Field, B. J. Murray, and K. S. Carslaw, 2018: Strong control of Southern
726 Ocean cloud reflectivity by ice nucleating particles. Proceedings of the National Academy of
727 Sciences, doi: 10.1073/pnas.1721627115.
728
729 Wegener, A.,: Thermodynamik der Atmosphäre, J.A. Barth Leipzig, 331 pp., 1911.
730
731 Winker, D. M., M. A. Vaughan, A. Omar, Y. Hu, and K. A. Powell, 2009: Overview of the CALIPSO
732 Mission and CALIOP data processing algorithms, Journal of Atmospheric and Oceanic
733 Technology, 26, 2310-2323, DOI:10.1175/2009JTechA1281.1.
734

Table Captions.

Table 1. Occurrence Statistics of Fully Attenuating Oceanic Columns Analyzed Between 40°S and 75°S Between January 2007 and December 2010 segregated by layer thickness and presence of precipitation.

Table 2. Occurrence Statistics of Surface-Based Lidar Layers Based in the MBL with base temperatures < 0°C.

Table 3. Values for the parameterization of ice occurrence fraction, *f,* of the blue and red dashed lines in Figure 4. The latitudinal boundary between north and south is taken to be 52°S

Figure Captions

Figure 1. The latitudinal distribution of surface based data showing the number of hours of measurements as described in the legend. The red bars show the total number of hours surface-based lidar data are available in that latitude bin. Green shows the number of hours with an identifiable cloud base. Cold clouds are those with a layer top temperature colder than freezing where the top is from coincident W-Band radar. Precipitating layers are those with W-Band radar reflectivity greater than -20 dBZ below the lidar cloud base.

Figure 2. Frequency of occurrence as a function of layer top temperature of Top) mixed-phase clouds layers for different layer thicknesses as described in the inset, Middle) fraction of time precipitation is diagnosed to be liquid when precipitation is observed, Bottom) The frequency of precipitation. Dashed curves are for satellite observations (CALIPSO and CloudSat) and solid curves represent data collected from ship-base lidars and W-Band radars

Figure 3. The occurrence frequency of mixed phase cloud from CALIPSO for MBL clouds of 1-3 km depth with top temperatures between -40C and 0C. The red curve shows the annually average location of the Antarctic Polar Front (APF), as reported in Freeman and Lovenduski, (2016). The black contours show where the confidence interval in the frequencies of occurrence are 25% of the value. The 95% confidence intervals as a fraction of the observed values are shown in the bottom frequency distribution.

Figure 4. As in the top panel of Figure 2 except we separate the CALIPSO data (top) and surface data (bottom) by latitude. Also shown (black dashed line) is the phase parameterization introduced by Kay et al., 2016. The red and blue dashed lines in the bottom panel show 1-*f* of the parameterizations of the phase occurrence derived from the ship-based data described by Equation 1 and Table 3.

779 Figure 5. Distributions of layer maximum dBZ from cloudsat in 1-3 km thick clouds between -
780 20°C and 0°C for all layers (black) and layers where CALIPSO observes mixed phase conditions.
781
782

783 Table 1. Occurrence statistics of fully-attenuating oceanic columns observed by CALIPSO
784 between 40°S and 75°S from January 2007 through December 2010 segregated by layer
785 thickness and presence of precipitation.

Occurrence Statistics of Space-Based Fully Attenuating Lidar Layers Based in the MBL with layer top temperatures < 0°C			
Layer Thickness	Layers Fully Attenuating (Fraction of Total Fully Attenuating Layers)	Precipitating Layers (Fraction of total layers in thickness range)	MPC (Fraction of Precipitating Layers in thickness range)
0-1 km	0.39	0.14	0.0
1-3 km	0.49	0.71	0.03
3-5 km	0.11	0.97	0.09
Total	16,485,317	0.51	0.04

786
787 Table 2. As in Table 1 except for layers observed from surface lidars during the CAPRICORN I,
788 CAPRICORN II and MARCUS voyages.

Occurrence Statistics of Surface-Based Lidar Layers Based in the MBL with layer top temperatures < 0°C. ALL Layers seen by radar (attenuating)			
Layer Thickness	Layers Fully Attenuating (Fraction of Total Fully Attenuating Layers)	Precipitating Layers (Fraction of total layers in thickness range)	MPC (Fraction of Precipitating Layers in thickness range)
0-1 km	0.64	0.18	0.30
1-3 km	0.25	0.58	0.62
3-5 km	0.11	0.66	0.82
Total	55,119	0.33	0.55

789
790
791
792 Table 3. Values for the parameterization of ice occurrence fraction, *f,* of the blue and red
793 dashed lines in Figure 4. The latitudinal boundary between north and south is taken to be 52°S

region	T_{ice} (K)	M (K^{-1})	T_{cold} (K)	f_{warm}	f_{cold}
North warm (NW)	273	90	262	0	N/A
North cold (NC)	262	40	238	$f_{nw}(T=T_{cold})$	1
South (S)	268	40	238	0	1

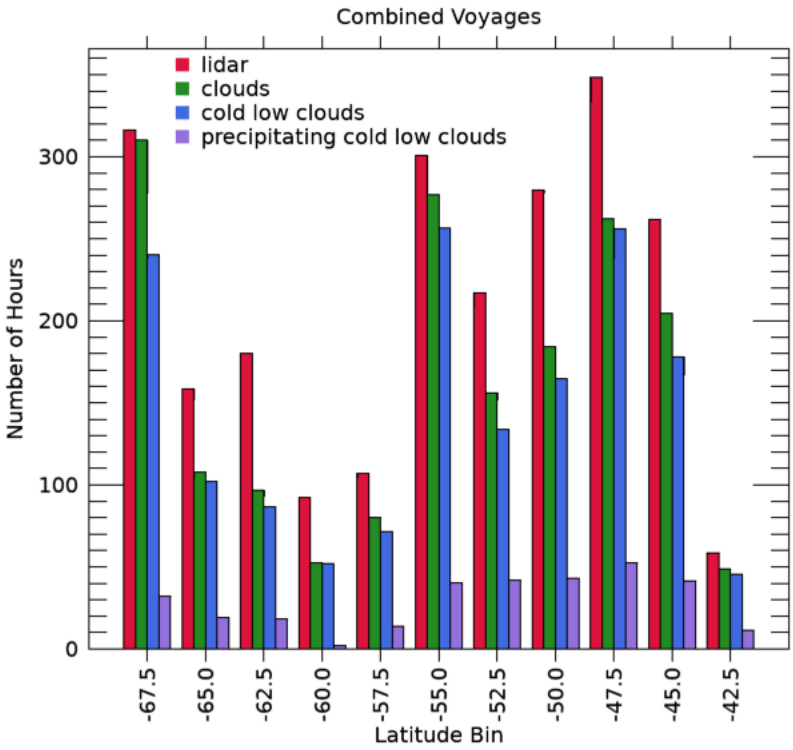

Figure 1. The latitudinal distribution of surface based data showing the number of hours of measurements as described in the legend. The red bars show the total number of hours surface-based lidar data are available in that latitude bin. Green shows the number of hours with an identifiable cloud base. Cold clouds are those with a layer top temperature colder than freezing where the top is from coincident W-Band radar. Precipitating layers are those with W-Band radar reflectivity greater than -20 dBZ below the lidar cloud base.

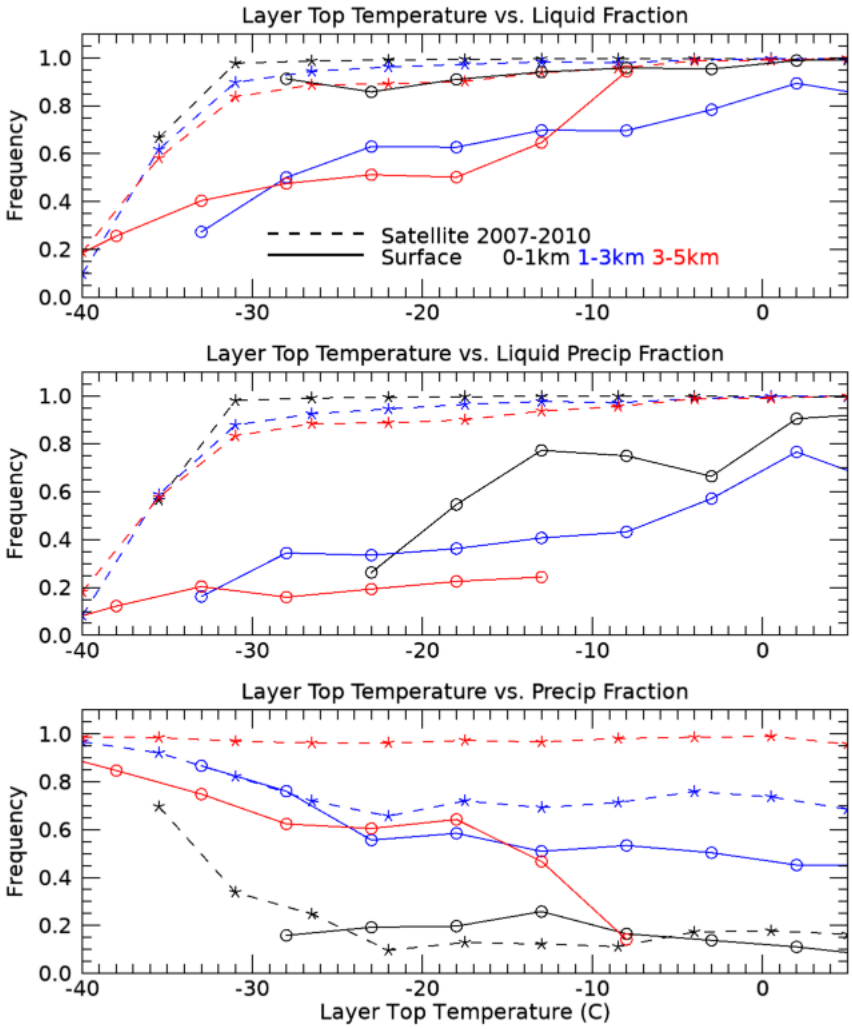

Figure 2. Frequency of occurrence as a function of layer top temperature of Top) mixed-phase clouds layers for different layer thicknesses as described in the inset, Middle) fraction of time precipitation is diagnosed to be liquid when precipitation is observed, Bottom) The frequency of precipitation. Dashed curves are for satellite observations (CALIPSO and CloudSat) and solid curves represent data collected from ship-base lidars and W-Band radars

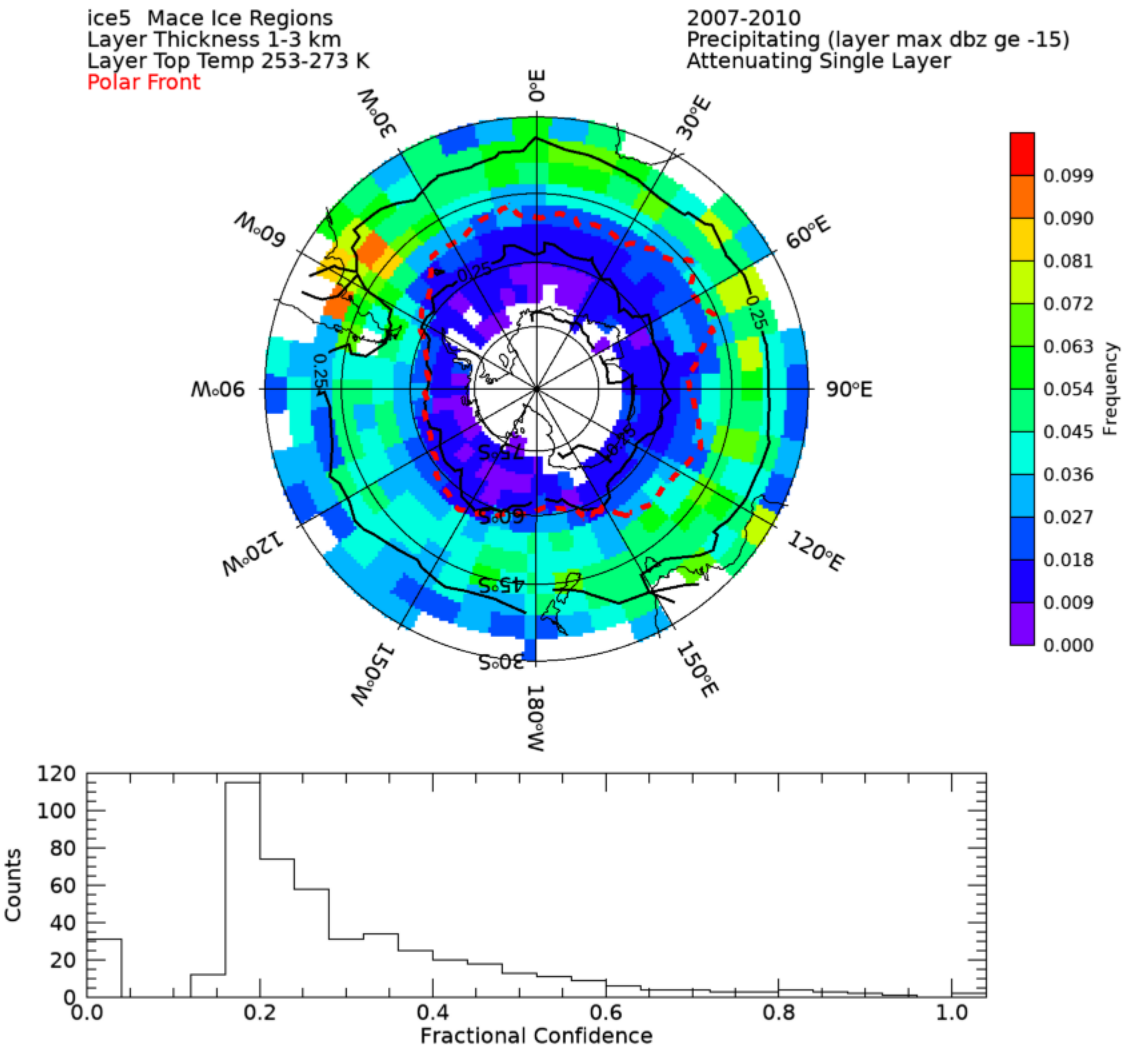

Figure 3. The occurrence frequency of mixed phase cloud for precipitating layers observed by CALIPSO and CloudSat for clouds based below 2 km and of 1-3 km depth with top temperatures between -20C and 0C. The red curve shows the annually averaged location of the Antarctic Polar Front (APF), as reported in Freeman and Lovenduski, (2016). The black contours show where the confidence interval in the frequencies of occurrence are 25% of the value. The 95% confidence intervals as a fraction of the observed values are shown in the bottom frequency distribution.

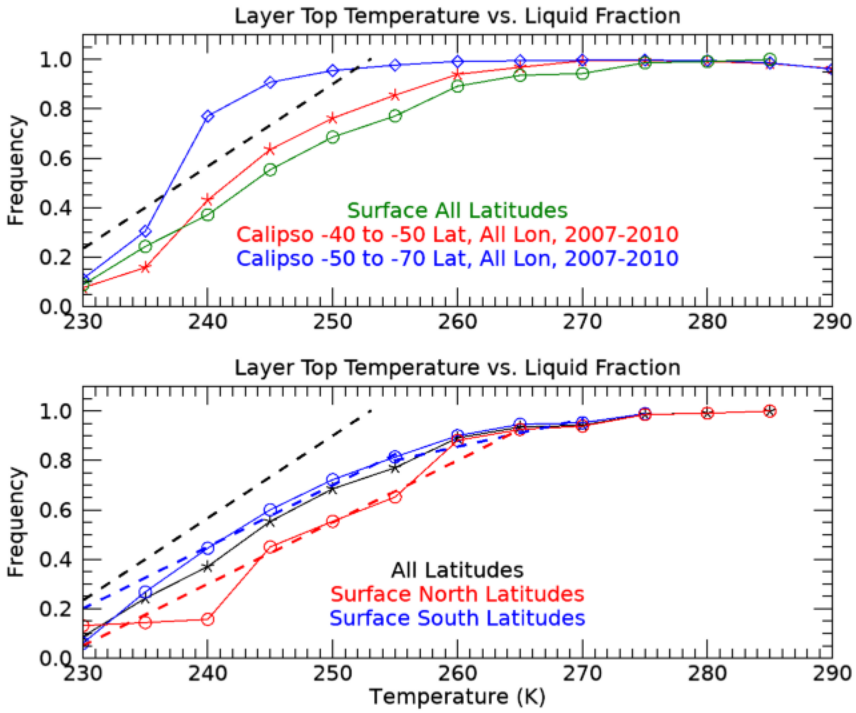

825
826
827 Figure 4. As in the top panel of Figure 2 except we separate the CALIPSO data (top) and surface
828 data (bottom) by latitude. Also shown (black dashed line) is the phase parameterization
829 introduced by Kay et al., 2016. The red and blue dashed lines in the bottom panel show 1-*f* of
830 the parameterizations of the phase occurrence derived from the ship-based data described by
831 Equation 1 and Table 3.
832

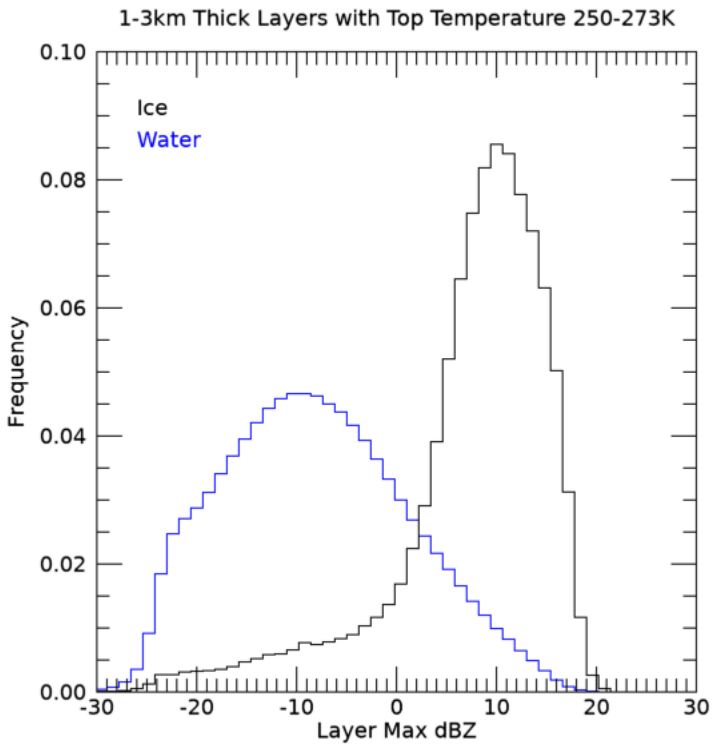

Figure 5. Distributions of layer maximum dBZ from cloudsat in 1-3 km thick clouds between -20°C and 0°C for all layers (black) and layers where CALIPSO observes mixed phase conditions.

Figure 1.

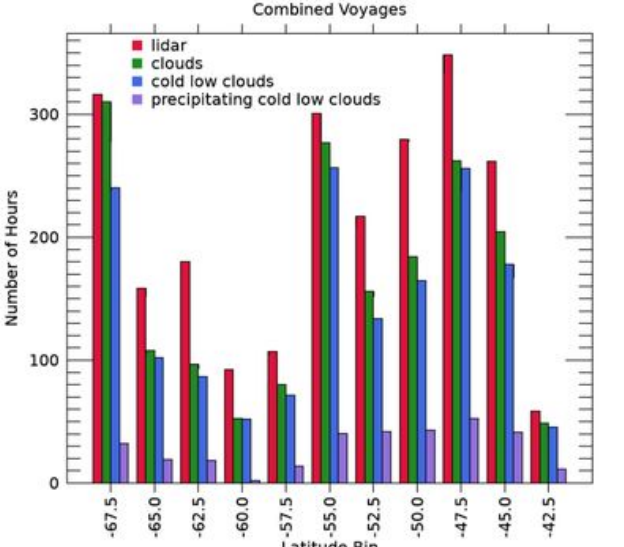
Combined Voyages
lidar
clouds
cold low clouds
precipitating cold low clouds
Number of Hours
0
100
200
300
-67.5
-65.0
-62.5
-60.0
-57.5
-55.0
-52.5
-50.0
-47.5
-45.0
-42.5
Latitude Bin

Figure 2.

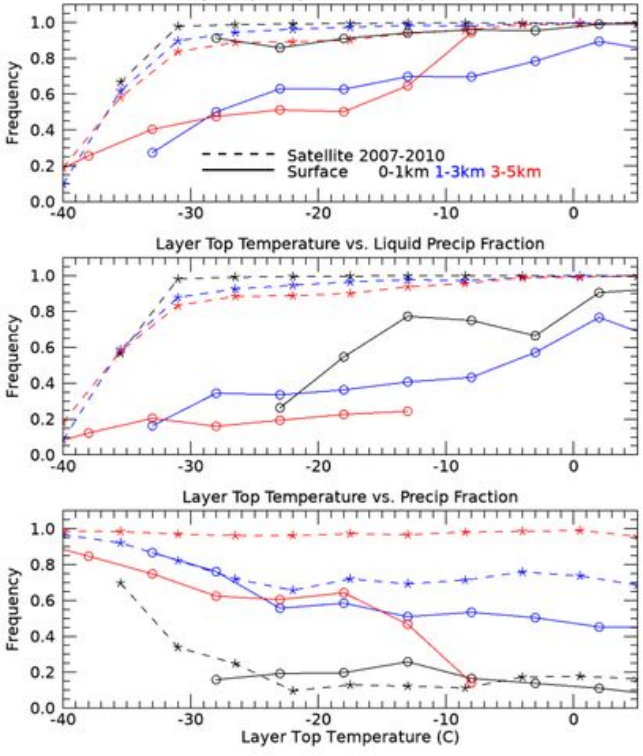
Layer Top Temperature vs. Liquid Fraction
Frequency
Satellite 2007-2010
Surface 0-1km 1-3km 3-5km
Layer Top Temperature vs. Liquid Precip Fraction
Frequency
Layer Top Temperature vs. Precip Fraction
Frequency
Layer Top Temperature (C)

Figure 3.

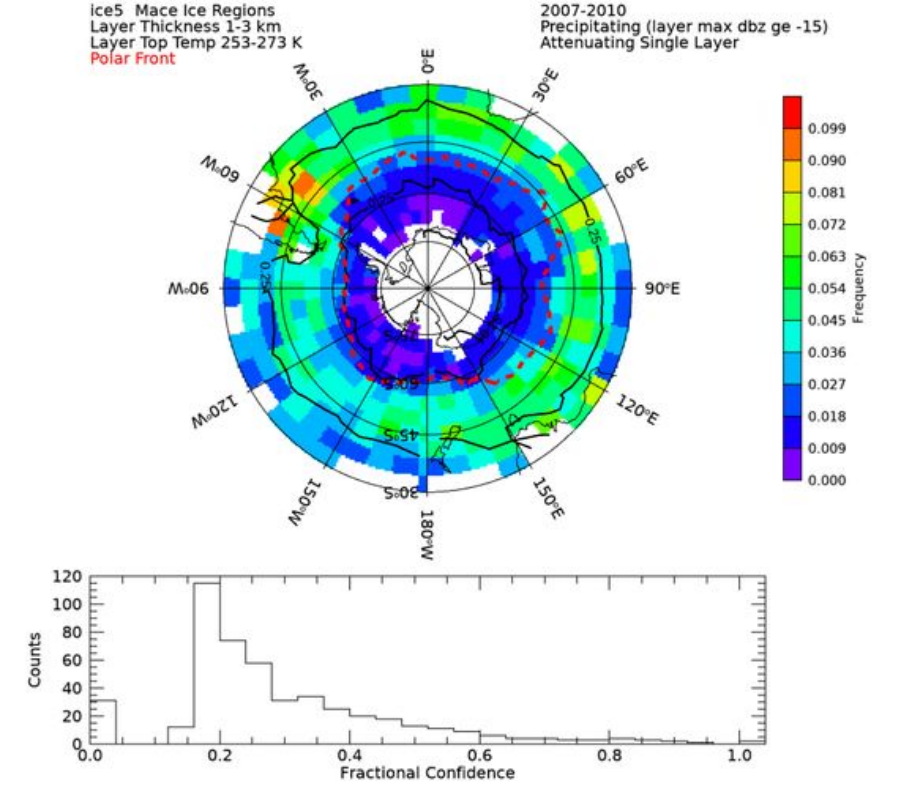
ice5 Mace Ice Regions
Layer Thickness 1-3 km
Layer Top Temp 253-273 K
Polar Front
2007-2010
Precipitating (layer max dbz ge -15)
Attenuating Single Layer
0°E
30°E
60°E
90°E
120°E
150°E
180°W
150°W
120°W
90°W
60°W
30°W
0.25
0.25
0.25
0.25
0.099
0.090
0.081
0.072
0.063
0.054
0.045
0.036
0.027
0.018
0.009
0.000
Frequency
Counts
Fractional Confidence
0.0
0.2
0.4
0.6
0.8
1.0
0
20
40
60
80
100
120

Figure 4.

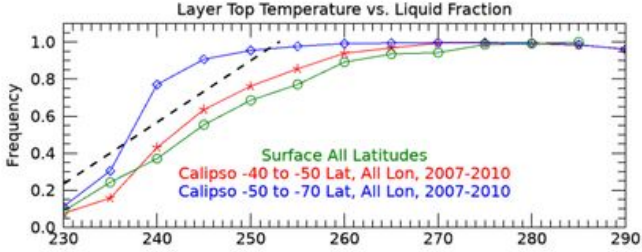
Layer Top Temperature vs. Liquid Fraction
Frequency
1.0
0.8
0.6
0.4
0.2
0.0
230
240
250
260
270
280
290
Surface All Latitudes
Calipso -40 to -50 Lat, All Lon, 2007-2010
Calipso -50 to -70 Lat, All Lon, 2007-2010

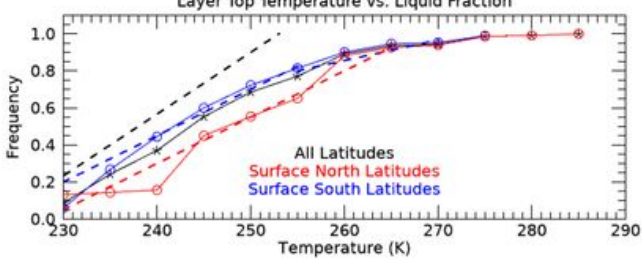
Layer Top Temperature vs. Liquid Fraction
Frequency
1.0
0.8
0.6
0.4
0.2
0.0
230
240
250
260
270
280
290
Temperature (K)
All Latitudes
Surface North Latitudes
Surface South Latitudes

Figure 5.

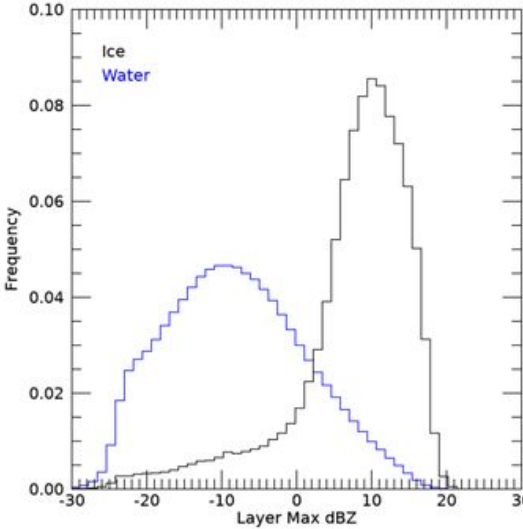
1-3km Thick Layers with Top Temperature 250-273K
Ice
Water
Frequency
0.10
0.08
0.06
0.04
0.02
0.00
-30
-20
-10
0
10
20
30
Layer Max dBZ